

## The formation mechanisms for mid-latitude ice scarps on Mars

K.E. Williams<sup>a,\*</sup>, C.M. Dundas<sup>a</sup>, M.A. Kahre<sup>b</sup>

<sup>a</sup> U.S. Geological Survey, Astrogeology Science Center, 2255 N. Gemini Dr., Flagstaff, AZ 86001, USA

<sup>b</sup> NASA Ames Research Center, Moffett Field, CA 95035, USA

### ARTICLE INFO

#### Keywords:

Mars  
Ice  
Scarps

### ABSTRACT

Mid-latitude exposed ice scarps have recently been identified on Mars (Dundas et al., 2018, 2021). The presence of such surface ice exposures at relatively low latitudes was itself a mystery, and the evolutionary dynamics of such scarps have also not been explained. In this work, we model the ice ablation rates of several identified mid-latitude scarps. We find that, given certain characteristics of their geographic setting, the orientation and growth of the scarps can be explained by energy balance models.

### 1. Background

The thermodynamic stability of ice on Mars has been a subject of intense interest since the early work by Leighton and Murray (1966). Much of the early work concerning ice stability was model-based, but there has been much recent observational research as well. Models indicate that ice should be stable at shallow depths at mid and high latitudes, with the depth to ice and latitude of the stability boundary dependent on the near-surface atmospheric water vapor content and the temperature of the shallow subsurface. Several recent models incorporating detailed information about thermophysical properties have produced global maps, which have moderately different assumptions but are broadly similar (e.g., Mellon et al., 2004; Schorghofer and Aharonson, 2005; Chamberlain and Boynton, 2007). Thermally derived maps are consistent with this theoretical picture (Bandfield and Feldman, 2008; Piqueux et al., 2019), and gamma ray and neutron spectrometer data are as well (e.g., Boynton et al., 2002). New small impact craters exposing ground ice also show a similar distribution (Byrne et al., 2009; Dundas et al., 2014, 2021).

Pore-filling ice is a natural consequence of deposition from diffusion of atmospheric water vapor (e.g., Mellon and Jakosky, 1993). A surprise from the last two decades has been increasing evidence for excess or massive ice: subsurface ice with little lithic material included. The initial indication of such cleaner ice was from Gamma-Ray Spectrometer data (Boynton et al., 2002) and this has subsequently been supported by much additional evidence including excavation by the Phoenix lander (e.g., Feldman et al., 2004; Smith et al., 2009; Mellon et al., 2009; Dundas and Byrne, 2010; Mouginot et al., 2010). This ice requires some additional process, most likely either snowfall and frost accumulation (e.

g., Madeleine et al., 2009, 2014) or various forms of near-surface ice lens formation or in situ growth (e.g., Fisher, 2005; Sizemore et al., 2015). Radar sounding has also detected evidence for local debris-covered glaciers in some locations (e.g., Holt et al., 2008; Plaut et al., 2009).

Recently, there has been evidence that parts of the Martian mid-latitudes contain not just a minor component of clean ice, but decameters-thick shallowly buried ice deposits, exposed in places in pole-facing scarps (Dundas et al., 2018). This is consistent with earlier radar evidence (Bramson et al., 2015; Stuurman et al., 2016) revealing ice sheets with coarser resolution and less detail. Models have suggested that ice deposition could be widespread at high obliquity (e.g., Madeleine et al., 2009, 2014) and these sheets may be the preserved remnants (e.g., Schorghofer and Forget, 2012; Bramson et al., 2017), although the specific history remains to be determined.

The scarps are bluer than their surroundings in enhanced-color images from the High Resolution Imaging Science Experiment (HiRISE; McEwen et al., 2007). They characteristically face slightly ( $10\text{--}20^\circ$ ) east of due poleward, with moderate variability both between scarps and on individual scarps encompassing some sections that face just west of poleward (Dundas et al., 2021). The scarps range up to several kilometers long and form the pole-facing wall of pits of similar dimensions and are tens to hundreds of meters high (Dundas et al., 2021). Typical slopes are  $45\text{--}50^\circ$  (Dundas et al., 2021).

According to Dundas et al. (2018), the exposures are a component of sublimation-thermokarst features, where sublimation starts in a specific location and curious landforms develop as a result. In particular, these thermokarst features often have a roughly triangular appearance, where the pole-facing scarp is one edge of the triangle, and two other edges are facing slightly east and west (Fig. 1). Morphological features of the

\* Corresponding author.

E-mail address: [kewilliams@usgs.gov](mailto:kewilliams@usgs.gov) (K.E. Williams).

scarps imply that they retreat in a straight line. This contrasts with roughly oval scalloped depressions, which are also thought to form via sublimation (Dundas et al., 2015a) but have distinctly different morphology (Fig. 2). For level ground at 55.2°S, 109.4°E (Fig. 1), Mellon et al. (2004) indicate that the depth to stable ice is only a few tens of cm deep. Ice is likely present in the shallow subsurface beneath all of the pit walls, but only occurs at the surface under the straight pole-facing scarp.

These pole-facing scarps pose several puzzles. First, it is surprising that an active sublimation feature should focus on the retreat of the pole-facing (coldest) slope; scalloped depressions have been successfully modeled by retreat of the warmer (i.e., equatorward-facing) slopes (Dundas et al., 2015a, 2015b). The scarps are pole-facing and receive little direct insolation. If they are in frequent shadow, the scarp must certainly be very cold (relative to the opposing slopes, which are illuminated for a longer portion of the day). How quickly does the cold pole-facing scarp sublimate and retreat? An estimate from Dundas et al. (2018) suggested that the retreat rate of one scarp is on the order of millimeters/Mars year, based on multiple meter-scale boulders falling from the scarp over three Mars years together with the frequency of exposed boulders within the icy matrix.

Perhaps the most surprising aspect of the pole-facing scarps in Figs. 1 and 2 is the fact that they are composed of cleanly exposed ice (i.e., ice not under a sublimation lag). If the scarp is actively sublimating, a lag deposit should rapidly accumulate. As a thought experiment, one meter of ice with one vol% dust would accumulate a two-cm lag upon sublimation if the lag has 50% porosity. This is easily enough to mask the ice from view and provide substantial protection against further sublimation, but this is not observed, even though >100 m of ice must have been lost to produce some observed pit depths, and the pit dimensions imply lateral retreat over kilometers. This is a challenge for both initiating scarps and for maintaining them once formed. Possible reasons that the slope remains exposed include either a) strong winds removing the lag as it develops, or b) the scarp is steep enough, and has sufficiently low lithic content, that the lag slides off, possibly aided by seasonal frost effects (Dundas et al., 2021). The first scenario is unlikely to be the sole explanation because winds are unlikely to be so similar at multiple sites, over both hemispheres, that the exposed slopes always have similar orientation and morphology. Instead, many of the scarps do indeed have piles of dust present at the foot of the slope. The one scarp with high-resolution topographic data analyzed by Dundas et al. (2018) is at a slope typically >45°, exceeding the angle of repose for most loose granular materials. Moreover, many of the scarps have scarp-parallel ridges at the base (Fig. 1D, 2B). There are often multiple ridges or linearities, suggesting a periodicity or episodicity to the erosional/depositional environment within the pit (Fig. 3). This could be due to climate variations influencing the retreat rate, and/or to variations inherent to the scarp evolution.

We hypothesize that: (i) the scarps remain free of a lag because they

are sustained at a slope too steep for lag material to accumulate, and (ii) under some conditions, the slope shallows enough that a lag does accumulate, producing a ridge within the pit, before becoming reactivated. Under this hypothesis, the pits would be sublimation-thermokarst landforms. Here we focus on understanding (i), and primarily on understanding the favored slope angles, as slope angle strongly affects insolation and thus sublimation rate. If the upper part of the scarp retreats faster than the lower part, the overall slope will fall and eventually reach a point where dust released by sublimation does not slough off, building a lag. The converse would allow the slope to steepen and grow, remaining free of dust cover. Part (ii) suggests that the ridges could be markers related to recent climate variations. However, a variant possibility is that the scarp spacing, and development of a lag, are determined simply by material accumulating upwards from the base of a scarp, similar to bedrock behind a talus slope. In this case the ridges would not be primarily paleoclimate indicators, but instead indicators of the dust content of the icy unit.

Within this framework, the retreat rate and favored slope angles are critical elements for understanding the scarp history and formation process. Scarp sublimation is expected to be strongly dependent on scarp latitude, slope angle, and aspect, given that these characteristics affect both the duration and intensity of incident sunlight. Therefore, we examine retreat rates at a range of scarps in this paper.

## 2. Observational constraints on scarp retreat

Dundas et al. (2018) estimated a retreat rate of several mm per Mars year for a southern hemisphere scarp (specifically, the site labeled southern scarp #2 by Dundas et al. (2021)). This estimate was based on the observation that several meter-scale boulders fell from the scarp over several Mars years. This scarp is the only one where numerous embedded boulders are visible in HiRISE images. An updated version of this calculation is now possible with additional data. An estimated 111 rocks were visible on the scarp face in HiRISE image ESP\_057782\_1245 (repeated counts gave slightly different numbers due to the ambiguity of identifying boulders at the limit of resolution, but this source of error is minor compared with other assumptions described below). At least six of these boulders shifted or could not be identified in comparison with ESP\_014161\_1245, acquired five Mars years earlier, suggesting that ~1% of the embedded rocks fall out per Mars year. The rocks are typically 0.5–1 m diameter. Assuming that a rock falls when it is 50–75% exposed and that the rocks are distributed uniformly within the ice, this suggests a retreat rate of 2.5–7.5 mm per Mars year for this scarp.

This estimate is subject to significant uncertainty which is difficult to quantify formally. Some rocks are likely not counted because they are not yet exposed enough to protrude significantly, and some of the falling rocks may be loose on the surface, having previously fallen but not rolled entirely off the scarp. These factors are poorly constrained by current

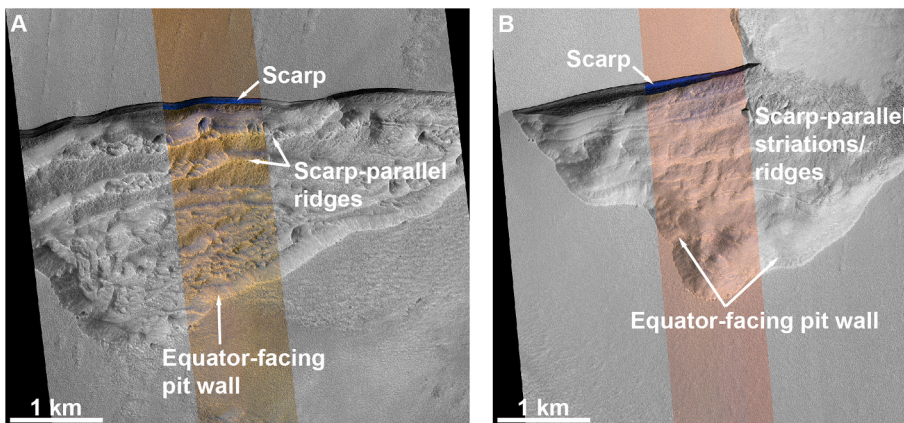


**Fig. 1.** Examples of triangular sublimation-thermokarst with sharp pole-facing scarps that expose ice. The sharp south- (pole-)facing slopes, blue in enhanced color, are exposed ice which can be over 100 m thick. A) South1 (notation of Dundas et al., 2021), with prominent ridges paralleling the scarp (56.6°S, 114°E). B) South2, with subtle low-relief ridges or striations (55.2°S, 109.4°E). (A: HiRISE image ESP\_056819\_1230. B: HiRISE image ESP\_057782\_1245. North is up and light is from the left in both panels. Latitudes are planetocentric. For color see the electronic version of the article; color swath is shown in darker gray in print.) (For interpretation of the references to color in this figure legend, the reader is referred to the web version of this article.)

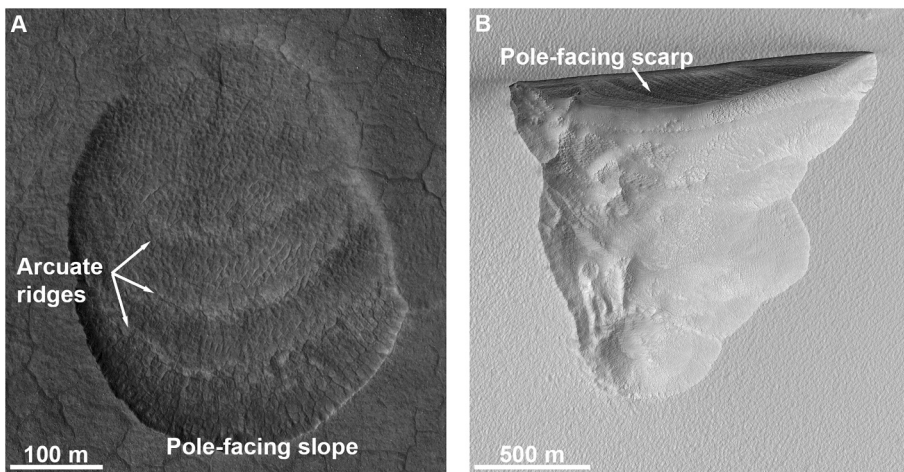


**Fig. 2.** Two types of sublimation-thermokarst features. A) A sub-circular scalloped depression in Utopia Planitia, located in the northern hemisphere ( $46^{\circ}\text{N}$ ,  $92.1^{\circ}\text{E}$ ). B) A triangular feature located in the southern hemisphere ( $56.8^{\circ}\text{S}$ ,  $96.3^{\circ}\text{E}$ ), exposing a straight icy scarp at the north end. The arcuate ridges in the scalloped depression contrast with the straight-line retreat of the exposed scarp. (A: HiRISE image PSP\_001938\_2265. B: HiRISE image ESP\_057466\_1230. North is up and light is from the left in both panels. Latitudes are planetocentric.)

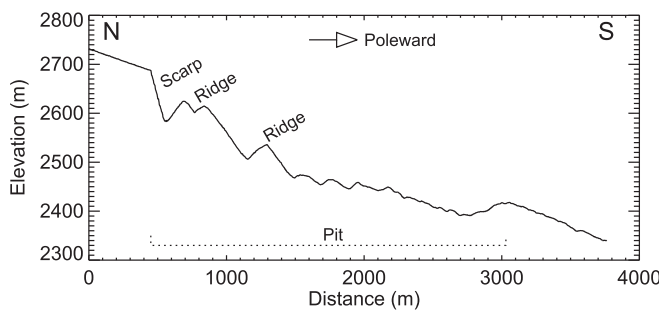


**Fig. 3.** An example of a transect across South1 (Fig. 1a) and the associated multiple transverse ridges from a HiRISE Digital Terrain Model (DTM). This scarp is paralleled by two substantial ridges that are likely ice-cored (as they stand above the floor of the pit) and several smaller ridge structures. These ridges may reflect previous positions of the scarp where it became buried and protected by a lag and may shrink over time as the ice core sublimates. Terrain profile is the same data as profile A-A' in Dundas et al. (2018), redrawn and annotated here.

data but on balance they are most likely to make the retreat rate lower than the estimate above.

The other major constraint on the scarp retreat is that the scarps retain icy coloration and spectral features throughout the Martian summer, although they may change slowly (Dundas et al., 2018). The quantitative meaning of this is dependent on both the dust content of the scarp and the processes that remove a lag from the surface. The thickness of an opaque dust lag may be as little as tens of microns (e.g., Wells et al., 1984; Fischer and Pieters, 1993). The combination of ablation rate, lag removal rate, and dust content in the ice must be consistent with these results. As a guide to intuition, assuming a lag porosity of 50%, ice with 1 vol% dust would produce a  $100\ \mu\text{m}$ -thick opaque lag after sublimation of 5 mm, assuming no mass wasting or other removal processes. For the retreat rate estimated above from boulder falls, this would be consistent with accumulation of a partially opaque lag within one summer unless dust removal occurs simultaneously. This is consistent with waning strength of water ice spectral features over the course of a summer at southern scarp #1 (Dundas et al., 2018).

### 3. Observational constraints on scarp slopes

Surface slope and aspect are critical inputs for thermal modeling. Dundas et al. (2021) made estimates of the slopes of several scarps based on the orientation of slopes that were just barely self-shadowing and estimated the scarp aspect as orthogonal to the trend of a line connecting

the scarp endpoints in non-orthorectified images. Since that time, high-resolution Digital Terrain Models (DTMs) have become available for South2, 3, 6, and 7, North4, and parts of North1, in addition to the previously available South1, enabling improved estimates. (Numbering herein corresponds to Dundas et al. (2021) but abbreviates, e.g., southern scarp #1 as South1.) We made measurements of slope and aspect by downsampling the DTMs to 10 m/post and then creating slope and aspect maps. Averaging to 10 m/post minimizes the effects of noise at small scales in the DTMs. We collected slope and aspect data for all points that were not within 10 m of the scarp edge, to avoid those that may have partially sampled the off-scarp surface. Results are presented in Table 1.

At South1, 2, and 3, and North1, where both DTM measurements and shadow estimates could be made, the mean slopes from the DTM are slightly less than (but within  $\sim 5^{\circ}$  of) the shadow-based estimates of Dundas et al. (2021). The latter estimates are easily within the range of the DTM slopes, so this likely indicates that the shadow method preferentially picked out locations that are slightly steeper than average. The scarp aspects from the DTMs are also similar to the estimates from the plan-view trend in Dundas et al. (2021), but slightly closer to due poleward. Overall, these results indicate that the slope and aspect values estimated by Dundas et al. (2021) are reasonable estimates but, unsurprisingly, are less accurate than measurements with a high-resolution DTM.

At South1, where there are prominent ridges paralleling the scarp, the surface slopes of the ridges are variable but  $<26^{\circ}$ . The debris-covered plinth at the base of the scarp is somewhat concave, and slopes at the transition from debris to exposed ice are mostly  $30\text{--}35^{\circ}$  but sometimes lower. Lower values are mostly observed where the plinth is not well-defined and scarp merges into the opposing slope via higher-standing terrain. As the angle of repose of lithic materials is commonly  $30\text{--}35^{\circ}$ , these observations are consistent with the overall model of scarp evolution proposed above: the scarp remains exposed because it is steep, while detached ridges and the basal slope are covered by debris below the angle of repose. Thus, we next turn our attention to understanding the controls on scarp slope.

### 4. Model

We model the scarps using a 2-d model of ice mass balance, composed of three coupled 1-d models (Fig. 4). Given that some of the scarps being studied have smaller transverse ridges at their foot and that the roughly triangular depression planform is not universal, we have simplified the general model approach as follows. The model consists of a large poleward-facing slope, and in one case we also include a smaller equatorward-facing slope at the foot. The slope angle and the precise

**Table 1**

Scarp slope and aspect statistics, derived from DTMs. Additional information, including locations, can be found in Table 2.

Scarp ID	DTM	N <sub>points</sub>	Slope ± std. dev (range)	Aspect ± std. dev (range)
South1	DTEEC_021466_1230_021954_1230_A01	2626	46.5 ± 2.1 (37.8, 53.9)	176.1 ± 8.0 (148.6, 193.5)
South2	DTEEC_057782_1245_057571_1245_A01	2484	46.8 ± 2.4 (33.6, 53.5)	175.6 ± 4.0 (164.7, 184.7)
South3	DTEEC_057809_1215_057598_1215_A01	671	43.2 ± 3.9 (35.8, 54.2)	180.2 ± 3.6 (172.9, 193.4)
South6	DTEEC_057677_1230_057466_1230_A01	1403	42.2 ± 2.1 (32.5, 48.5)	182.8 ± 1.7 (176.0, 189.5)
South7	DTEEC_057677_1230_057466_1230_A01	704	39.1 ± 2.9 (29.5, 46.7)	171.8 ± 3.2 (162.8, 183.6)
North1t	DTEEC_053320_2345_053241_2345_A01	380	48.2 ± 2.0 (43.1, 54.7)	3.1 ± 5.1 (350.8, 18.7)
North1aa	DTEEC_071085_2345_071006_2345_A01	262	48.5 ± 5.1 (33.6, 58.5)	18.8 ± 4.9 (7.0, 42.7)
North4b	DTEED_018420_2375_017563_2375_A01	933	31.0 ± 3.9 (20.4, 41.9)	326.5 ± 9.8 (302.3, 354.1)

DTMs from the northern sites cover multiple scarps; results were similar for all, so we only present examples here. Standard deviations describe the spread of measurements and do not include other uncertainty such as map projection distortion (minor) or DTM noise. For the northern scarps, aspects straddle the 0–360° singularity, and were rotated prior to computing the mean to preserve a valid result.

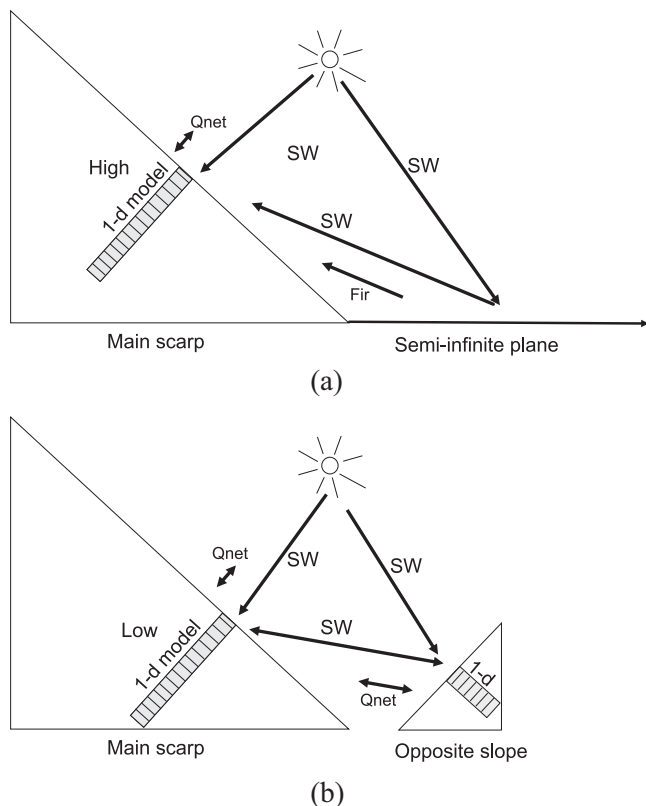


**Fig. 4.** General model diagram, indicating the three 1-d models coupled to form a 2-d model. Panel a is for the “High” configuration, and panel b. is the “Low” configuration. The main scarp is generally poleward facing, whereas the smaller opposite slope is 180° from the main slope aspect. Ablation rates are tracked at the “High” and “Low” positions on the slope. SW denotes short-wavelength insolation (direct and reflected).  $Q_{\text{net}}$  includes the following fluxes: latent heat, sensible heat, atmospheric heating (downwelling infrared radiation), and emitted infrared fluxes from opposing surfaces. Most cases of the model are equivalent to the High position on the main scarp, and thus do not include the effects of the small equatorward facing slope which is minor in most cases. Instead, the High position interacts with a semi-infinite plane at the foot of the main scarp with a soil surface temperature from the General Circulation Model (GCM) that is representative of the region.

aspect of both slopes are adjustable in the model. The model is applied to several key identified scarp locations identified in Dundas et al. (2021). The explicit finite-volume model is similar to that of Williams et al. (2008), where the 1-d ice column on the slope is comprised of 1250 ice layers with an average thickness of 2 cm (total of ~4 annual skin depths). The topmost layer is permitted to grow and shrink, and as it changes it may be subdivided and create a new upper layer or become

small enough to be combined with the underlying layer.

There are two model configurations: the model is configured to run at either a “Low” or “High” position on the main scarp. (Herein, “High” and “Low” always refer to position on the scarp, while steep and shallow indicate the slope angle.) All cases are run at the “High” position on the slope except South1, which has a prominent (but smaller) opposite scarp at the foot of the main scarp. The model calculates a surface energy balance, together with energy transfer in the subsurface. Both model positions (Low and High) are subject to the same general flux terms, including latent heat (sublimation), sensible heat, insolation (direct), atmospheric heating (downwelling IR), emitted IR and IR from the opposite slope. Geothermal flux was assumed to be zero since this has a negligible effect on surface temperature. The difference between Low and High positions concerns the source of incoming emitted IR and reflected SW radiation: either the opposite slope or a broad semi-infinite plane at the foot of the main scarp. The “Low” position is sufficiently low that it “sees” only the opposite slope, hence any incoming reflected insolation and emitted IR comes only from the opposite slope. The “High” position, on the other hand, only receives emitted IR and reflected SW from a semi-infinite plain at the foot of the slope, where we used the insolation equations of Mellon and Phillips (2001). This is a simplified and generalized topographic scenario that is best regarded as two end-members that illustrate the trend in scarp evolution as a function of position on the slope, which are themselves simplifications of the complex topography of pole- and equator-facing surfaces in view of the scarp. In particular, most scarps lack a prominent ridge immediately adjacent to the ice exposure. It will still generally be true that for a constant slope angle, the Low slope will have a larger solid angle of the input hemisphere occupied by the flat floor and opposing pit walls while the High slope has more solid angle occupied by cold sky. Moreover, near the base of the scarp more solid angle is likely to be occupied by small, nearby equator-facing slope facets.

Our model is driven by the NASA Ames Legacy Mars Global Climate Model (MGCM; Haberle et al., 2019) outputs of near-surface air temperature, relative humidity, wind, and downward visible and IR fluxes, and surface thermal inertia. Our modeling outcome (dependent variable) is the annual scarp H<sub>2</sub>O ice mass-balance. The MGCM simulation used a Mars Year 24 dust scenario (Montabone et al., 2015), which represents a typical year without a planet-encircling dust event. While planet-encircling dust events occur every one out of three years on average (Zurek and Martin, 1993; Smith et al., 2009), they have not been found to significantly affect global mean surface temperatures (e.g., Streeter et al., 2019). We initialize the ice column temperature profile in a two-step manner as follows: as a very rough first guess, we set the entire column to be the mean annual GCM-supplied ground surface temperature. Next, prior to integrating the annual loss rate, we complete a two-Mars-year spin-up for the ice column during which no loss is permitted (but all other surface energy budget terms are included). We elected to use two years for spinup given that we found that by the third year the loss rates had quickly approached an asymptotic value (ice has a high thermal conductivity).

We conducted radiative transfer calculations for ice to inform our assumptions about albedo and thermal inertia used in the modeling. Specifically, our calculations suggest that a dust concentration within the ice on the order of 10<sup>3</sup> ppm matches the average observed dust albedos. This high of a dust concentration would lead to nearly all the insolation being absorbed and reflected within the top computational ice layer. Hence, in the interests of faster model computation times, we elected to use a fixed albedo instead of a full radiative transfer calculation for each timestep. We used the observed regional albedo from the Thermal Emission Spectrometer (TES) for each scarp. The scarps are not resolved by this data set and may be somewhat brighter than the regional average, but this is difficult to quantify using HiRISE data without atmospheric and topographic corrections that are not possible in most cases. The effect of albedo is investigated as a sensitivity test below.

The calculation of sensible and latent heat is as follows. We compute the sensible heat flux as

$$Q_H = -\rho C_p u (T_a - T_s) \frac{k^2}{\left(\ln\left(\frac{z}{z_0}\right)\right)^2} \sqrt{F_h F_m} \quad (1)$$

where  $\rho$  is the atmospheric density (calculated as a function of air temperature),  $u$  is the wind speed,  $k$  is the Von Karman constant (0.4), and  $C_p$  is specific heat capacity of the atmosphere (840.9 J Kg<sup>-1</sup> K<sup>-1</sup>).  $T_a$  and  $T_s$  are temperatures of the atmosphere and surface, respectively. The atmospheric variables are measured at a height ( $z$ ) which is the lowest layer of the MGCM output, and  $z_0$  is the roughness length (discussed below).  $F_h$  and  $F_m$  are the stability functions for heat and momentum, defined by Hourdin et al., (1995). In this case the stability functions are functions of the Richardson number  $Ri = \frac{gz\Delta\theta}{T_u^2}$ , where the potential temperature gradient  $\Delta\theta \approx T_a - T_s$ ,  $g$  is gravity,  $z$  is the instrument height, and  $\bar{T} = \frac{T_a + T_s}{2}$ .

For  $Ri < 0$ , indicating unstable conditions:

$$F_m = (1 - 64Ri)^{\frac{1}{2}} \quad (2a)$$

$$F_h = (1 - 61Ri)^{\frac{1}{2}}$$

For cases where  $Ri \geq 0$ , indicating stable conditions:

$$F_m = \frac{1}{1 + 10\frac{Ri}{\sqrt{1+5Ri}}} \quad (2b)$$

$$F_h = \frac{1}{1 + 15\frac{Ri}{\sqrt{1+5Ri}}}$$

We calculate the latent heat flux as

$$Q_E = \rho L_v u (w - w_s) \frac{k^2}{\left(\ln\left(\frac{z}{z_0}\right)\right)^2} \sqrt{F_h F_m} \quad (3)$$

where  $w$  and  $w_s$  are the mass mixing ratio of water vapor in the air and the saturation mass mixing ratio at the ice surface, respectively, and the latent heat of vaporization is  $L_v$ . Note that the forced convective mass loss is simply Eq. (3) divided by  $L_v$ .

For free convective mass loss, where  $\geq Ri_c$ , we calculate using the Ingersoll (1970) formulation:

$$m_{free} = 0.17(e - e_{sat}) M_w \frac{D}{k_b T} \left[ \left( \frac{\Delta\rho_{air}}{\rho_{air}} \right) \left( \frac{g}{v^2} \right) \right]^{1/3} \quad (4)$$

where  $e$  and  $e_{sat}$  are the water vapor partial pressure in the atmosphere and saturation vapor pressure at the ice surface, respectively. Here  $k_b$  is the Boltzmann constant,  $T$  is the atmospheric temperature,  $g$  is gravity,  $M_w$  is the molecular weight of water and  $v$  is the atmospheric kinematic viscosity. The diffusivity of water vapor in CO<sub>2</sub> gas is calculated as  $D =$

$1.387 \times 10^{-5} \left( \frac{T}{273.15} \right)^{3/2} \left( \frac{10^5}{P} \right)$ , where  $P$  is atmospheric pressure (Chittenden et al., 2008). The remaining term is defined as

$$\frac{\Delta\rho_{air}}{\rho_{air}} = \frac{26e_{sat}}{(44P - 26e_{sat})}$$

Following Andreas (2002) for the case where  $Ri \geq Ri_c$ , we compute the sensible heat flux in this laminar stable regime as

$$Q_h = -\rho C_p D_t \frac{dT}{dz} \quad (5)$$

for thermal diffusivity  $D_t$  of CO<sub>2</sub>. There are at least two other formulations for Eq. (4) (Dundas and Byrne, 2010; Schorghofer, 2020). They are all fundamentally similar (to a factor of ~2), however, and in this study, we found that the atmosphere was rarely in a free-convective regime (where  $Ri \geq Ri_c$ ), and hence the mass loss results were essentially insensitive to the formulation of Eq. (4).

The sensible and latent heat fluxes from the scarp are calculated in a manner similar to that of the Ames MGCM, with one exception as explained below. We chose the Ames model approach for two reasons. The first is to ensure that the calculated surface fluxes were approximately consistent with the fluxes of the Ames MGCM forcing data, both in methodology and outcome. The second reason is that the Ames approach uses stability functions which are solely functions of the Richardson number (Ri), a practice which is widely used due to the simplicity of the calculation. The Richardson number (non-dimensional) is a standard method of determining atmospheric stability and is defined as the ratio of buoyancy to the turbulence generated by shear flow. When the Richardson number is negative the atmosphere is deemed unstable, close to zero indicates a neutral atmosphere, and a positive number indicates stability. The critical Richardson number  $Ri_c$ , a strongly stable condition beyond which fluid flow becomes mostly laminar due to turbulence being suppressed, is a subject of some debate for terrestrial work. We have elected to use a value of  $Ri_c = 1.43$ , as recommended in Andreas (2002). There is growing evidence that the use of lower critical Richardson numbers, such as 0.2 (the value used in the Ames MGCM), is not recommended given that turbulent eddies may still not be adequately suppressed until  $Ri > 1.0$  (Andreas, 2002).

For the stability functions, we used the same roughness length scale ( $z_0$ ) as the Ames model. The Ames model uses a value of  $z_0 = 0.1$  mm for ice surfaces (Haberle et al., 2019), which is somewhat lower than values used by most terrestrial researchers. In order that our surface fluxes are calculated in a manner consistent with the Ames MGCM, and since stability functions are moderately strong functions of  $z_0$ , we use a value of  $z_0 = 0.1$  mm. Roughness length scales are not dependent on idiosyncratic properties of a particular planetary atmosphere, but rather by the general logarithmic “law of the wall” and the size of surface roughness elements. Hence, for a given temperature and wind profile, there is no reason to believe that the momentum (or heat and vapor) roughness length scales would be different between one terrestrial planetary atmosphere and another, other than via differences in surface properties (surface roughness elements). Most of the terrestrial work on roughness lengths of ice surfaces finds  $z_0$  length scales ranging between <0.1 mm to 80 mm (Brock et al., 2006), with the majority of lengths on the order of 1 mm.

For validation of the ice model, we modeled the accumulation of CO<sub>2</sub> frost depths over flat (level) ground for a latitude of 60°S and found excellent agreement with the observations of Kelly et al. (2006). While our estimated maximum CO<sub>2</sub> frost depth was larger than Kelly et al. (2006) predicted, our timing of the CO<sub>2</sub> frost deposition and removal was extremely close (less than a few degrees of LS) to Kelly et al. (2006). For a thermal model, the timing of the presence of CO<sub>2</sub> frost is more critical than replicating the exact depth because the presence of CO<sub>2</sub> frost will pin the temperature to the frost point.



**Table 4**

Model sensitivities for the South2 “High” configuration. The largest sensitivities were scarp slope angle, followed by the aspect angle.

Sensitivity case	Loss rate (mm/Mars yr.)	Model sensitivity (%)
Base case (South2, High)	2.4	n/a
Albedo of slope $\pm 10\%$	2.6 / 2.2	9 / 8
Scarp slope angle $\pm 4.8^\circ$	3.6 / 1.7	47 / 28
Scarp aspect angle $\pm 8^\circ$	1.9 / 3.5	22 / 43
Ice T profile instead initialized to mean annual air T in ABL	2.4	~0

the natural variability on an individual scarp in addition to the uncertainty from inaccurate parameter inputs. South2 was designated as the baseline case, and our results indicate that the primary model sensitivities are the scarp slope and aspect angle. The model is less sensitive to albedo and thermal inertia estimates. Initializing the ice temperatures to be the mean annual air temperature from the GCM (instead of the mean annual ground surface temperature from the GCM) had a very slight effect, but it was less than the designated model precision of 0.1 mm/yr. These estimates suggest that while the parameter uncertainties and natural variability are significant, they do not affect order-of-magnitude conclusions and thus our basic results are robust. The largest uncertainty is likely the greater complexity of real scarps.

## 7. Controls on scarp morphology and evolution

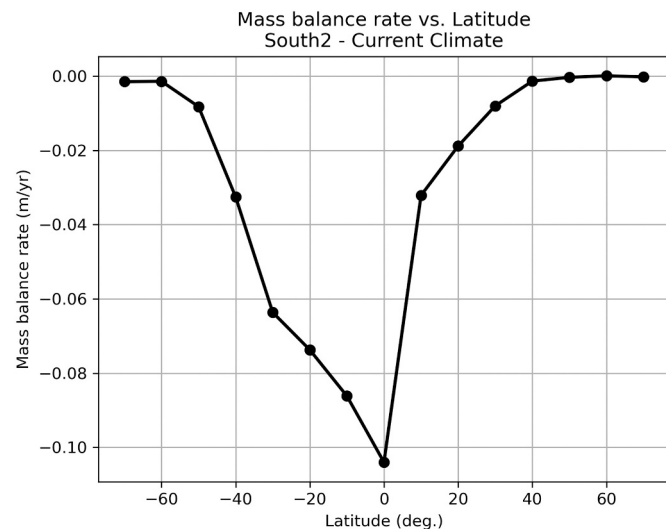
Because the modeled retreat rate is quite sensitive to slope and aspect, a scarp with variable slope and aspect will evolve in shape. Scarps on the pole-facing sides of pits are expected to evolve towards the geometry with the slowest retreat rate and thus develop a straight geometry. This is because in a sub-circular pit, the pole-facing slope is overall concave towards the pole. If the scarp matches this concave geometry, the east- and west-facing sides of the scarp extend in front of the center, but also retreat faster. They therefore draw back into line with the pole-facing slope while widening the scarp, driving the system towards a linear scarp face and triangular shape.

To understand the physical controls on scarp formation and evolution, we conducted additional model runs using the slope configuration of South2 but with systematic variations of particular properties. Because this variation is ad hoc, the precise values are not likely to be accurate for these experiments; instead, we use these to demonstrate trends that can explain observed scarp properties. South2 is at a latitude of  $-55^\circ$  and longitude of  $109^\circ\text{E}$ . When calculating loss rates for these sensitivity tests are in the northern hemisphere, we invert the slope orientation so that it has an aspect of  $4.4^\circ$ .

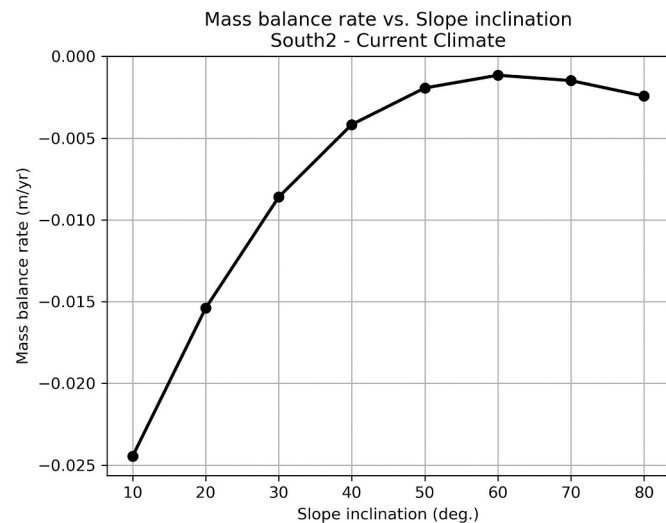
Fig. 5 shows scarp retreat rate as a function of latitude. As expected, retreat rates are very high near the equator. The observed scarps only occur at higher latitudes where the retreat rates are relatively low. This suggests a likely latitudinal control: scarps can only occur where sublimation is not so rapid that they are erased.

Fig. 6 shows the retreat rate for South2 as a function of slope. The retreat rate has a minimum near  $60^\circ$ . This value is slightly steeper than typical of current scarp estimates, but broadly similar in view of the model uncertainties and simplifications. In combination with the Low versus High results where the lower slope retreats faster than the upper, this suggests that concave-up scarp slopes steepen until they minimize their loss rate, and the exposure geometry is controlled by this equilibration. It is likely that the nominal equilibrium slope and profile varies somewhat with latitude and other properties and is also influenced by shadowing of the base of the slope by the upper section, not captured by our model.

Figs. 7 and 8 show retreat rates as a function of slope aspect. In both hemispheres, the minimum retreat rate occurs for a slope slightly east of due poleward. This explains the observed eastward bias of scarp orientations from Dundas et al. (2021).



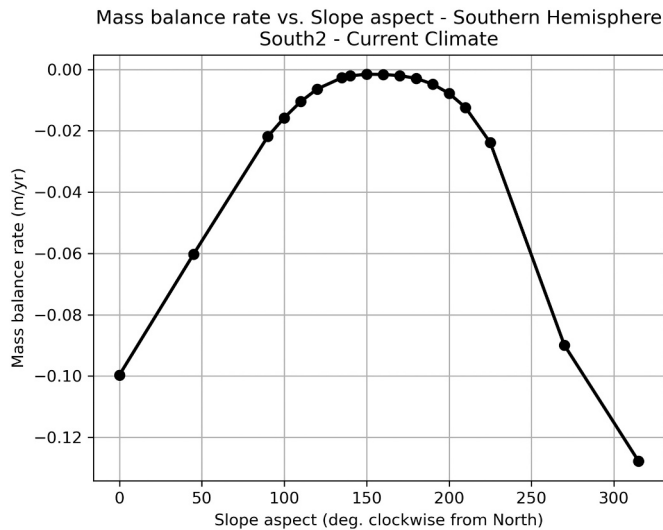
**Fig. 5.** Loss rate vs latitude for South2. In the northern hemisphere, South2 has an aspect of  $11^\circ$  (i.e., it is pole-facing in each hemisphere). The two hemispheres are not mirror images of one another, due to a seasonal asymmetry from the timing of perihelion.



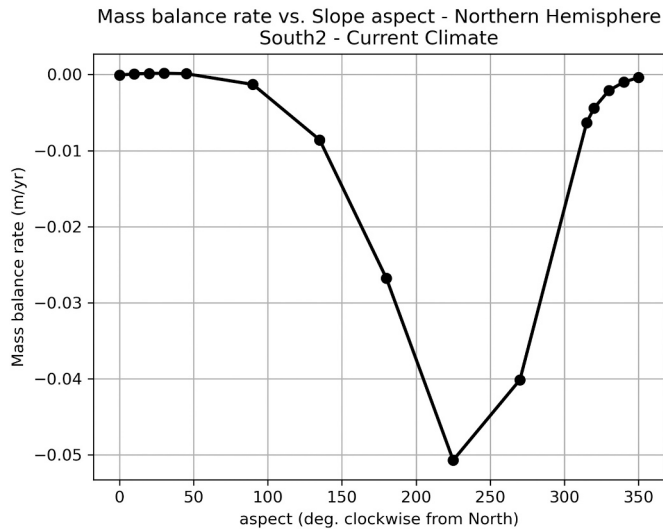
**Fig. 6.** Loss rates for South2 at various slope inclinations.

Fig. 9 shows the slope geometries conducive to scarp preservation (lowest loss rates), as a function of latitude, slope and aspect. As indicated in Fig. 9, the most favorable slope and aspect depend on latitude. Again, we posit that oversteepened slopes (beyond the angle of repose for loose dust) are likely to be self-cleaning, due to the combined effects of frost, wind, and mass wasting. In addition, it is likely that they will be self-correcting in slope angle, given that steeper slopes will experience greater radiation from nearby adjacent surfaces (e.g., ridges at the foot of the scarp), increasing the overall icy scarp loss rates. Modeling in Fig. 9 does not include any additional radiative contributions from basal ridges.

For a latitude of  $-55^\circ$ , similar to Scarp 2, Fig. 9B and C suggest that slopes between  $40^\circ$  and  $80^\circ$  with aspects between  $140^\circ$  to  $180^\circ$  are likely to be created and preserved. The lack of scarps at high latitude, despite the likely presence of massive ice, may be explained by this model: the equilibrium slope at  $70^\circ\text{S}$  latitude is distinctly lower (Fig. 9D) and given model uncertainties may fall below the angle of repose, suggesting that similar exposures at high southern latitude would quickly bury themselves in their own debris. Extremely high minimum retreat rates at



**Fig. 7.** Loss rates for South2 for various slope aspects in the Southern Hemisphere. The lowest loss rates in the southern hemisphere are for slopes facing 140–180°.



**Fig. 8.** Loss rates for South2 for various slope aspects in the Northern Hemisphere. The northern hemisphere minima occur on slopes facing between 350 and 50°.

lower latitudes (40°S) may preclude the formation of any well-defined pseudo-equilibrium scarp, or there may simply be a lack of suitable ice bodies. The true equilibrium slope will be influenced not only by the configuration that minimizes retreat rate but also by the relative rates of the upper and lower parts of the slope, which is not fully captured by Fig. 9.

## 8. Past climates

Using a high-obliquity run of the Ames MGCM for driving the scarp model, we have modeled scarp loss rates for a hypothetical Martian climate of obliquity = 35° and longitude of perihelion ( $L_{sp}$ ) = 270° as shown in Fig. 10. This corresponds to high-obliquity conditions of the last 1–2 Ma (Laskar et al., 2004). The GCM simulation for this case used the current-day value for eccentricity, the same dust scenario as the current Mars case (the MY 24 dust scenario), and radiatively inert water ice clouds. Again, Fig. 10 modeling does not include the additional radiative contribution from any basal ridges or complex opposing slopes.

Retreat rate is dramatically higher in the southern hemisphere for these orbital parameters, for all latitudes and slopes. Raw data are provided in supplemental online material for the current climate plots, as well as other past climate scenarios (obliquity = 35°,  $L_{sp}$  = 90°; obliquity = 15°,  $L_{sp}$  = 90°; and obliquity = 15°,  $L_{sp}$  = 270°). In general, we find that loss rates are much greater at high obliquity, particularly when perihelion coincides with summer, and much lower at low obliquity.

## 9. Discussion

For the present climate, we model scarp retreat rates of order 1–10 mm/year in the southern hemisphere, and successfully match the retreat rate within reasonable uncertainties for the one scarp where it has been quantitatively constrained by observations. The rates are rough estimates given necessary model simplifications and observational limitations, so order-of-magnitude agreement is the best possible with current observed data; it suggests that we are sufficiently capturing the basic physics of scarp evolution. In the northern hemisphere, retreat rates are predicted to be very low for pole-oriented scarps, possibly consistent with the scarps being in equilibrium and not actively changing in the present climate. If so, this would likely reverse on ~25 kyr timescales when perihelion aligns with southern summer.

This model for scarp evolution rates also successfully explains several aspects of their morphology. Notably, it predicts a steep equilibrium slope at the latitudes where scarps have been observed, consistent with maintaining a clean surface not buried under its own debris. It also predicts a slight eastward skew in scarp orientations.

The proposed process for creation of linear scarps depends on their pole-facing aspect. For an overall equator-facing ice exposure, the opposite feedback would occur, as the equator-facing slope would retreat fastest and increase scarp plan-form concavity. However, for moderate to low obliquities at mid-latitudes the upper part of such a slope may receive more direct insolation than the base, due to shadowing. The slope would be reduced during retreat and become too shallow to shed debris, resulting in burial of the scarp. This is similar to the likely evolution scenario for scalloped depressions, which have been modeled to form by retreat of the equator-facing slope beneath a debris lag too thin to stabilize ice (Dundas et al., 2015a, 2015b). The formation of pole-facing ice scarps, scalloped depressions, and/or expanded craters thus likely reflect different combinations of initial geometry, mass wasting rate, and local ice stability conditions influencing which slopes are most active.

Scarp sublimation rates are strongly influenced by climate and therefore by climate variations, which in recent times have largely been driven by changes in Mars' orbit and obliquity. The first-order age estimates in Table 3 must be inaccurate, as all of the astronomical parameters have varied significantly within the longest of the projected scarp lifetimes, and  $L_{sp}$  has reversed several times within the shortest. The near order-of-magnitude range in those timescales does suggest that the scarps have initiated at different times, rather than at some specific climate event or transition; since the scarps are mostly geographically clustered, the relative variations in age and retreat rate are likely reasonable even if the absolute values are incorrect. While our model does not make any prediction about scarp origins, this may be consistent with initiation via stochastic disturbances such as impact craters, coupled with climate conditions favorable for scarp formation/evolution. Fig. 11 shows a possible example of this: a small scarp in a near-circular pit that could be a degraded impact crater.

In the model of Laskar et al. (2004), the obliquity of Mars has been <27° for ~400 ka, with many excursions to near 35° between 0.5 and 1.5 Ma. The combination of extremely high retreat rates predicted at 35° obliquity and the higher ages in Table 3 produces a self-inconsistent history. If the scarps were old enough for those rates to have occurred, they would rapidly have formed the full size of the scarp pits even in the limited windows where high obliquity and summer  $L_{sp}$  coincide, but that would render the age estimates that permit such high retreat rates

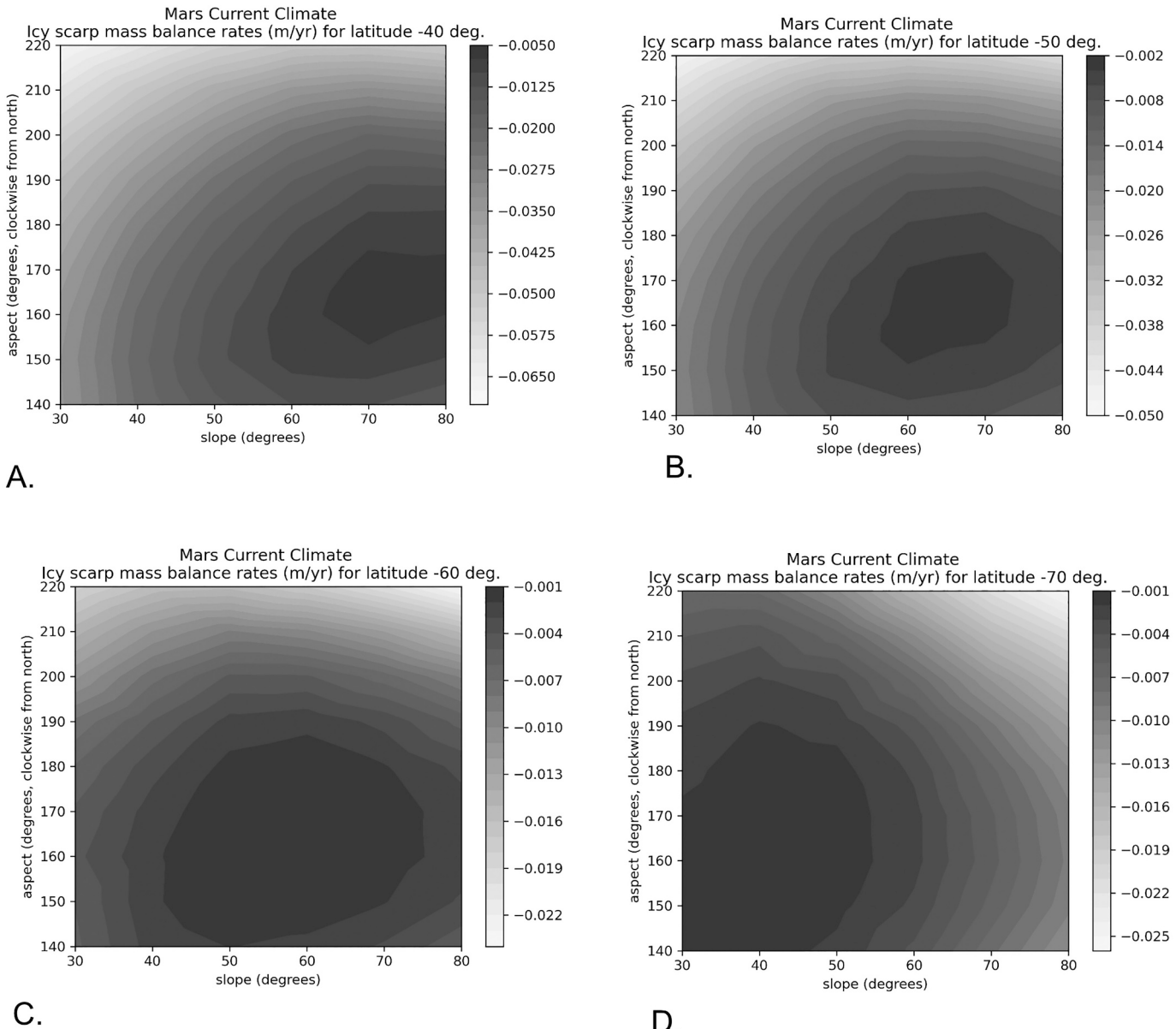


**Fig. 9.** Icy scarp loss rates as a function of slope and aspect, for the current Mars climate of obliquity = 25° and longitude of perihelion ( $L_{sp}$ ) = 251°. Darker areas indicate geometries conducive to scarp preservation. Raw data are provided in supplemental online material.

incorrect. It is more likely that the scarps are somewhat younger than the timescales in Table 3 and mostly postdate the era of high obliquity excursions, although the older scarps may have initiated during an era with modestly higher obliquity peaks, permitting a self-consistent combination of ages and retreat rates. Evolution of  $L_{sp}$  also drives variation over time with northern and southern scarps alternating in peak intensity of evolution. South1 and 2 both have particularly well-defined parallel features indicating past scarp positions, which could be consistent with particularly strong climate variations in their lifetime although not enough to change the favored orientation, and also have the oldest ages in Table 3.

Unfortunately, model uncertainties for both paleoclimate and for scarp retreat rate are sufficient that we cannot derive unique histories. We examined the present climate, as well as four simulations considering summer and winter perihelion at obliquities 15° and 35°. These are sufficient to show that (i) scarp retreat is faster at higher obliquity, and (ii) scarp retreat is faster for summer perihelion. There are numerous other poorly constrained variables, such as atmospheric dust loading

and the past location of surface ice deposits. This set of simulations is useful for understanding trends with those two variables, but the parameter space for past climate is large, and there remains moderate uncertainty about even the instantaneous retreat rates in the present climate.

Given that the model predicts rapid scarp retreat at high obliquity, why would scarps *not* date to that epoch? A range of factors might have prevented scarp initiation. One such factor is strong ice deposition, which might out-compete the steepening effects that allow scarps to grow, particularly if deposition is concentrated at the base of slopes (c.f. Conway and Mangold, 2013). This possibility is not captured by the paleo-GCM runs used herein, but there are significant uncertainties about both past climate and the timing of ice deposition. A reasonable assumption is that mid-latitude ice was deposited at higher obliquities (e.g., Madeleine et al., 2009, 2014), however Levrard et al. (2004) show ice deposition at similar latitudes for low obliquities. Other uncertainties regarding paleoclimate runs include dust loading, initial surficial ice reservoirs, and the surface ice albedo (which is a function of surface dust

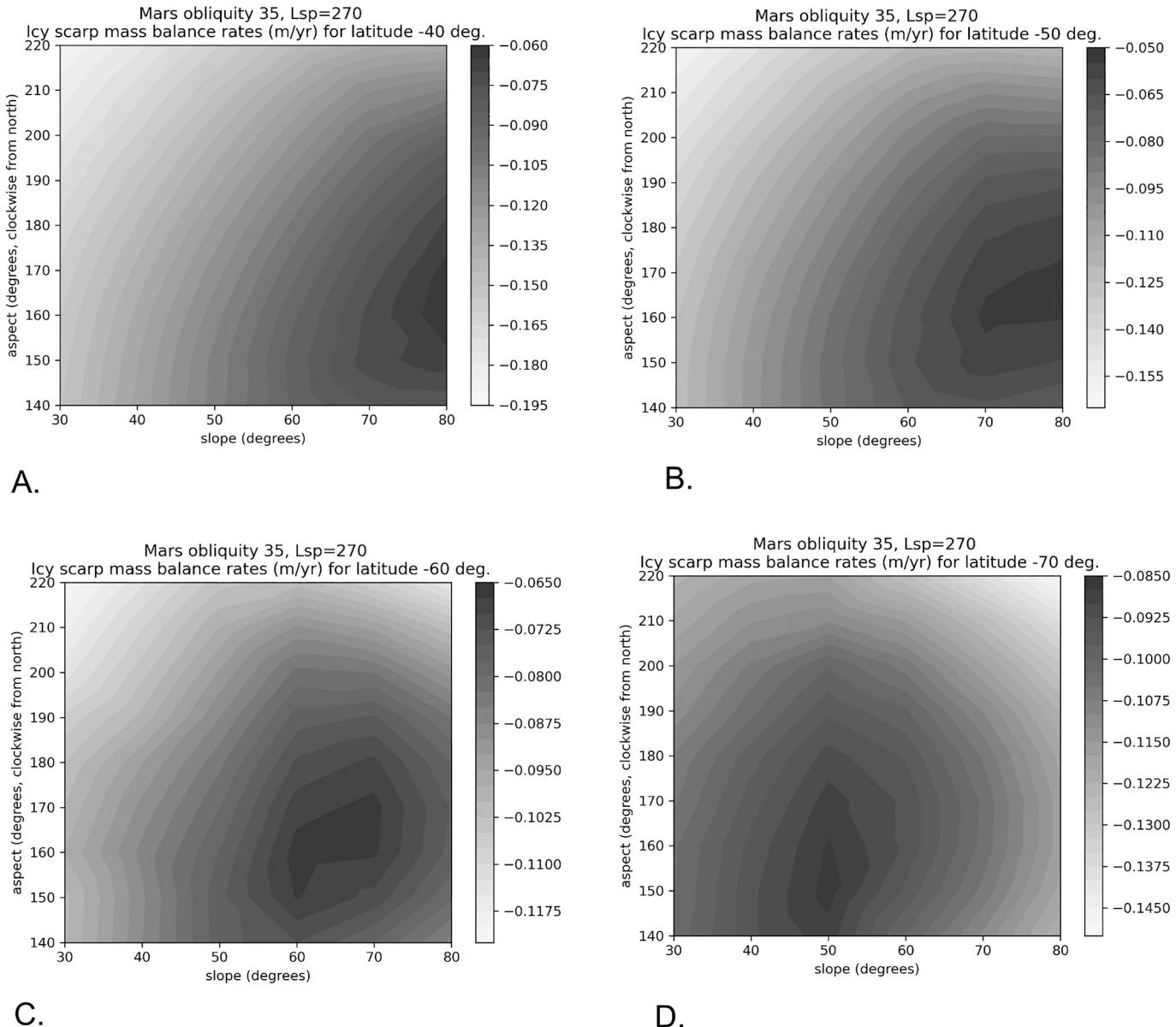


**Fig. 10.** Icy scarp loss rates as a function of slope and aspect, for a hypothetical past climate of obliquity = 35° and  $L_{sp} = 270^\circ$ . Darker areas indicate geometries conducive to scarp preservation. Raw data are provided in supplemental online material.

loading vs time). [Madeleine et al. \(2009\)](#) show mid-latitude glaciation at 35° obliquity, using radiatively inactive clouds and high atmospheric dust loading. [Madeleine et al. \(2009\)](#) used low-latitude water sources and high dust loadings year-round to stabilize ice at the mid-latitudes. In our simulations, however, the water source is at the pole and the dust loading varies seasonally. Hence, an additional possible factor in scarp evolution not captured by our model is the competition between ablation and new ice deposition. Additionally, some of the effects on scarp evolution described above that create the steep, linear shape may not apply at high obliquity. Specifically, the interactions of favored orientations and evolution of the upper and lower parts of scarps may break down. For instance, at 35° obliquity and  $L_{sp} = 90^\circ$  the minimum retreat rate is not on a strongly pole-facing slope. Finally, a more rapidly changing climate associated with higher-amplitude obliquity oscillations might prevent formation of a well-defined landform.

## 10. Conclusions

We modeled the evolution of steep ice exposures observed in the Martian mid-latitudes. In the southern hemisphere we estimate current retreat rates of  $\sim 1\text{--}10$  mm/Mars year, consistent with observations, while northern scarps appear to be near equilibrium and minimally retreating. This may be explained by the current coincidence of perihelion and peak temperatures for the southern scarps. Simplistic extrapolation of retreat rates in the south suggests landform ages of a few hundred ka to a few Ma, but scarp retreat is expected to strongly vary with obliquity and  $L_s$  of perihelion so those age estimates are likely too high, especially in the older cases. Scarp growth is explained by more rapid retreat rates of the lower scarps. Steep slopes are favored, creating the overall morphology that prevents the scarps from burying themselves under their own debris.



- Schorghofer, N., Forget, F., 2012. History and anatomy of subsurface ice on Mars. *Icarus* 220, 1112–1120. <https://doi.org/10.1016/j.icarus.2012.07.003>.
- Sizemore, H.G., Zent, A.P., Rempel, A.W., 2015. Initiation and growth of Martian ice lenses. *Icarus* 251, 191–210.
- Smith, P.H., et al., 2009. H<sub>2</sub>O at the Phoenix landing site. *Science* 325, 58–61.
- Streeter, P., Lewis, S., Patel, M., Holmes, J., Kass, D., 2019. Surface warming during the 2018/MY 34 Mars Global Dust Storm. In: Ninth International Conference on Mars. USRA, Pasadena, California, USA.
- Stuurman, C.M., Osinski, G.R., Holt, J.W., Levy, J.S., Brothers, T.C., Kerrigan, M., Campbell, B.A., 2016. SHARAD detection and characterization of subsurface water ice deposits in utopia Planitia, Mars. *Geophys. Res. Lett.* 43 (18).
- Wells, E.N., Veverka, J., Thomas, P., 1984. Mars: experimental study of albedo changes caused by dust fallout. *Icarus* 58, 331–338.
- Williams, K.E., Toon, O., Heldmann, J., McKay, C., Mellon, M., 2008. Stability of mid-latitude snowpacks on Mars. *Icarus* 196, 565–577. <https://doi.org/10.1016/j.icarus.2008.03.017>.
- Zurek, R.W., Martin, L.J., 1993. Interannual variability of planet-encircling dust storms on Mars. *JGR* 98, 3247–3259.